PROCEEDINGS OF SPIE

SPIEDigitalLibrary.org/conference-proceedings-of-spie

Visualization of shocked material instabilities using a fast-framing camera and XFEL four-pulse train

Hodge, Daniel, Pandolfi, Silvia, Liu, Yanwei, Li, Kenan, Sakdinawat, Anne, et al.

Daniel Hodge, Silvia Pandolfi, Yanwei Liu, Kenan Li, Anne Sakdinawat, Mathew Seaberg, Philip Hart, Eric Galtier, Dimitri Khaghani, Sharon Vetter, Chandra B. Curry, Franz-Joseph Decker, Bob Nagler, Hae J. Lee, Cindy Bolme, Kyle Ramos, Pawel M Kozlowski, David S. Montgomery, Matthew S. Dayton, Leora Dresselhaus-Marais, Suzanne Ali, Liam D. Claus, Marcos O. Sanchez, Thomas Carver, Richard L. Sandberg, Arianna Gleason, "Visualization of shocked material instabilities using a fast-framing camera and XFEL four-pulse train," Proc. SPIE 11839, X-Ray Nanoimaging: Instruments and Methods V, 1183908 (8 September 2021); doi: 10.1117/12.2594216

SPIE.

Event: SPIE Optical Engineering + Applications, 2021, San Diego, California, United States

Downloaded From: https://www.spiedigitallibrary.org/conference-proceedings-of-spie on 10 Dec 2021 Terms of Use: https://www.spiedigitallibrary.org/terms-of-use

Visualization of Shocked Material Instabilities Using a Fast-Framing Camera and XFEL Four-Pulse Train

Daniel Hodge[a], Silvia Pandolfi[b], Yanwei Liu[b], Kenan Li[b], Anne Sakdinawat[b], Mathew Seaberg[b], Philip Hart[b], Eric Galtier[b], Dimitri Khaghani[b], Sharon Vetter[b], Chandra B. Curry[b], Franz-Joseph Decker[b], Bob Nagler[b], Hae J. Lee[b], Cindy Bolme[c], Kyle Ramos[c], Pawel M. Kozlowski[c], David S. Montgomery[c], Matthew Dayton[d], Leora Dresselhaus-Marais[d*], Suzanne Ali[d], Liam D. Claus[e], Marcos O. Sanchez[e], Thomas Carver[f], Richard L. Sandberg[a], Arianna Gleason[b]

[a]Brigham Young University, Department of Physics and Astronomy, Provo, UT, USA, 84602
[b]SLAC National Accelerator Laboratory, 2575 Sand Hill Rd, Menlo Park, CA, USA, 94025
[c]Los Alamos National Laboratory, Los Alamos National Laboratory, Los Alamos, NM, USA, 87545
[d]Lawrence Livermore National Laboratory, 7000 East Ave, Livermore, CA, USA, 94550
[e]Sandia National Laboratories, 1515 Eubank Blvd SE, Albuquerque, NM, USA, 87123
[f]Stanford Nano Shared Facilities, Stanford University, Palo Alto, CA, USA, 94305
[*]Current Affiliation: Stanford University, Department of Materials Science, 450 Serra Mall, Stanford, CA, USA, 94305

Abstract. Many questions regarding dynamic materials could be answered by using time-resolved ultra-fast imaging techniques to characterize the physical and chemical behavior of materials in extreme conditions and their evolution on the nanosecond scale. In this work, we perform multi-frame phase-contrast imaging (PCI) of micro-voids in low density polymers under laser-driven shock compression. At the Matter in Extreme Conditions (MEC) Instrument at the Linac Coherent Light Source (LCLS), we used a train of four x-ray free electron laser (XFEL) pulses to probe the evolution of the samples. To visualize the void and shock wave interaction, we deployed the Icarus V2 detector to record up to four XFEL pulses, separated by 1-3 nanoseconds. In this work, we image elastic waves interacting with the micro-voids at a pressure of several GPa. Monitoring how the material's heterogeneities, like micro-voids, dictate its response to a compressive wave is important for benchmarking the performances of inertial confinement fusion energy materials. For the first time in a single sample, we have combined an ultrafast x-ray framing camera and four XFEL pulse train to create an ultrafast movie of micro-void evolution under laser-driven shock compression. Eventually, we hope this technique will resolve the material density as it evolves dynamically under laser shock compression.

Keywords: Icarus V2, UXI, MEC, pulse, void-shock, heterogeneities, fusion, XFEL.

*Daniel Hodge, dhodge@byu.edu

1 Introduction

Studying transient behavior of matter in extreme conditions is vital to the understanding of the physical and chemical processes found in materials and in nature.[1–6] Imperfections at the micron scale influence the physical and chemical behavior of all materials, and it is thus crucial to understand how structural defects alter the materials response to extreme conditions. For example, it has been proposed that the growth of hydrodynamic instabilities, such as the Rayleigh-Taylor (RT) and Richtmeyer-Meshkov (RM) instabilities, at present,

X-Ray Nanoimaging: Instruments and Methods V, edited by Barry Lai, Andrea Somogyi, Proc. of SPIE
Vol. 11839, 1183908 · © 2021 SPIE · CCC code: 0277-786X/21/$21 · doi: 10.1117/12.2594216

Downloaded From: https://www.spiedigitallibrary.org/conference-proceedings-of-spie on 10 Dec 2021
Terms of Use: https://www.spiedigitallibrary.org/terms-of-use

prevents thermonuclear ignition in inertial confinement fusion (ICF) tests.[7–10] These instabilities along with implosion asymmetries contribute significantly to the degradation of materials performance in ICF implosions.[7,8] During recent experiments at the National Ignition Facility (NIF), degradation was observed when high-density carbon (HDC) ablator material mixed with the hot spot during the implosion, resulting in 'meteors' or bright spots in x-ray images.[9,10] It has been suggested that the occurrence of these 'meteors' might be caused by the presence of micro-voids in the HDC layer. Therefore, being able to image dynamic events at the critical nanosecond and sub-micron scale is important to understand the interaction of shock waves with structural defects, as they may play a crucial role in the seeding and growth of hydrodynamic instabilities that currently prevent ignition in ICF experiments.

To analyze how instabilities arise in shock-void interactions, we combined the four-pulse XFEL mode at LCLS, the Icarus V2 ultrafast x-ray imaging (UXI) camera, and laser-shock compression at the MEC instrument to analyze the evolution of microstructural heterogeneities under nanosecond laser-driven shock compression. In our experiment, an optical long-pulse laser produces shock waves that interact with a hollow silica shell void embedded in photoresist polymer SU-8 samples. To examine material performance in these extreme states, we used the LCLS XFEL four-pulse train and the Icarus V2 camera to collect x-ray phase-contrast images. The Icarus V2 detector is an ultrafast x-ray imaging (UXI) camera developed by Sandia and Lawrence Livermore National Laboratories for the study of high energy density physics (HEDP) experiments.[11] The fastest non-UXI cameras can capture images at 200 ns intervals, which is significantly slower than the dynamics of laser-shock compression on the order of a few nanoseconds. Here, with improved functionality, the Icarus V2 was deployed to record up to four XFEL pulses separated by 1-3 nanoseconds between each pulse, enabling us to directly visualize how material defects can contribute to the seeding and growth of hydrodynamic instabilities that evolve on the micron scale upon laser-driven shock compression (see Fig. 1). By combining UXI cameras with a train of high flux XFEL pulses (10^{12} photons/pulse) at the LCLS XFEL, potential 100 nm resolution images can be collected.[5,6,12–14] With the Icarus V2, we analyzed materials in the high pressure regime (several Mbar) and collected a series of up to four dynamic images separated by only a few nanoseconds that can provide novel insight on the formation and growth of instabilities in ICF materials.[15] In this work, we present the first application of multi-frame imaging from a XFEL pulse train to the Icarus UXI detectors.

Downloaded From: https://www.spiedigitallibrary.org/conference-proceedings-of-spie on 10 Dec 2021
Terms of Use: https://www.spiedigitallibrary.org/terms-of-use

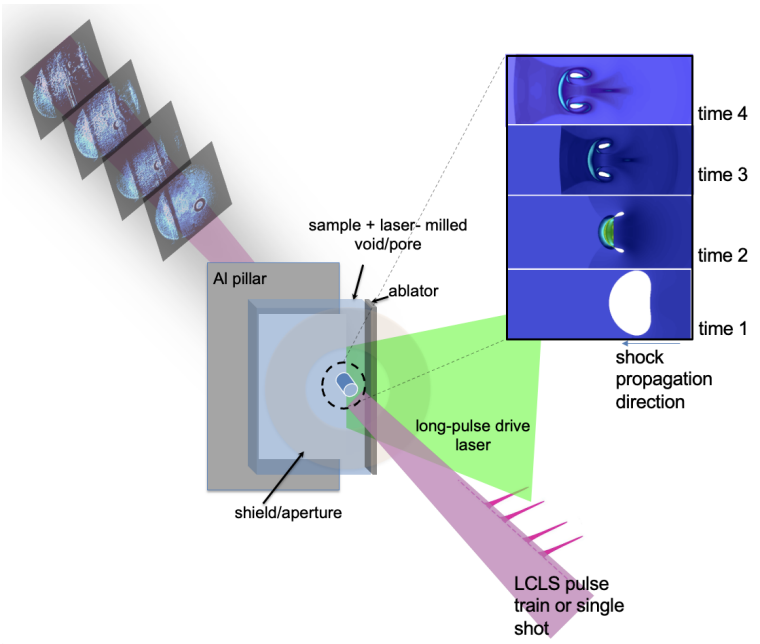


Fig 1 A schematic describing the experimental setup at the LCLS-MEC showing a four-pulse train illuminating a laser shock driven void in an SU-8 sample, generating a series of four x-ray phase-contrast images captured on the Icarus V2 camera. The upper right of the figure gives an example of changes in the void geometry. (Upper right inset adapted from ALE3D simulation,[16] LLNL.)

2 Detector Description

Sandia and Lawrence Livermore National Laboratories developed the UXI sensors that were used in our experiments.[11,17–20] For our experiment we implemented the Icarus V2 detector, which was housed in a 3D printed box. Triggering, data collection, and basic corrections, such as subtracting pedestals calculated from dark runs, were performed using standard LCLS tools.[21] The DAQ and camera timing setup were as described in Hart et al.[12]

The Icarus V2 sensor is a 1024 x 512 pixel, 4-frame burst-mode hybrid-CMOS sensor with 25 μm pixel pitch. It generates 4 unique and independently programmable shutters from an external asynchronous trigger and distributes these shutters on a row wise manner. The array is split timing wise into East and West hemispheres to allow for 2 independently timed arrays of 1024 x 256 pixels.[11,12,20] The detector operated in the 1-2 timing mode where there is a 1 ns gate followed by a 2 ns reset. In a previous experiment at LCLS, the Icarus V1 was implemented to record wide-angle diffraction signal from two XFEL pulses separated by 4.2 ns for an x-ray pump x-ray probe experiment to measure ultrafast x-ray heating in copper.[12] This experiment and others demonstrated the effectiveness and capability of UXI cameras in recording multi-frame material dynamics.[13,14,22]

The Icarus V2 camera is part of the UXI sensor family and it is a multi-frame hybridized complementary metal oxide semiconductor (CMOS) sensor.[11] It is 'hybridized'

Downloaded From: https://www.spiedigitallibrary.org/conference-proceedings-of-spie on 10 Dec 2021
Terms of Use: https://www.spiedigitallibrary.org/terms-of-use

because a custom readout integrated circuit (ROIC) is bonded to an array of silicon photodiodes, which are 25 μm in pitch and is sensitive to soft and hard x-rays.[20] The Icarus V2 can capture images on the nanosecond time scale utilizing MOSFET switches as electronic shutters.[11] These shutters remove readout speed limitations by storing these frames in-situ on in-pixel storage elements and then reading off the stored charge on a slower timescale.[18] The shutters, also known as the 'gate' in the context of UXIs, controls the pixel's integration time and gain.[20]

This type of camera can collect data at the speeds required for ultra-fast timescale experiments. The collection speed is dictated by how many memory elements can fit into a given pixel.[18] Essentially, each pixel has a buffer that acts as temporary storage for the intensity measured by that pixel. The transfer of charge from the pixel to this buffer and clearing the pixel is fast enough to record data within 1 ns.[18] The use of a UXI camera was crucial for the success of the in-situ experiments presented here.

3 Experimental Details

To study the shock-void wave interactions, we imaged the evolution of micro-voids within the sample with multiframe x-ray phase contrast imaging. We used a train of four x-ray pulses with pulse widths between 40-80 fs at 8.23 keV to observe micro-void compression in low density polymers at the sub-micron length scale (see Fig.1). For the first time, with the Icarus V2, we acquired a series of four x-ray phase-contrast images (XPCI) at the LCLS.

At the MEC instrument we used the 60 J, Nd:glass laser system to provide long-pulse laser ablation to shock our samples.[5,6] This system operates at 1054 nm and the pulse is split into two arms to eventually become frequency-doubled to 527nm.[5,6] The pulse-shaping capabilities at MEC allow users to produce laser pulses with duration ranging between 2 and 200 ns.[5,6] For two experimental runs (runs 292 and 295) we used a 10 ns quasi flat-top optical pulse. The laser was focused down to a 300 μm spot on the sample.

Figure 2 shows the temporal profile of the laser drive pulse that was used in our experiment. The main drive pulse was set to have a quasi-flat top square profile of 10 ns duration. The pulse profile recorded by the oscilloscope (Fig. 2) shows a temporal modulation that deviates from an ideal flat top shape. This effect has been mitigated later during the experiment by acting on the pulse slicer (Pockels cell). Furthermore, an additional low-intensity pulse was detected, as shown in the inset in Fig. 2. The presence of two distinct features in the driver profile, i.e., a low-intensity pre-pulse preceding the main laser pulse, results in a double-stage compression. An initial shock at moderate pressure is launched through the sample, followed by the main compression shock wave. The signature of both the low- and high-pressure shock have been identified in the PCI images, as discussed in the following section.

Downloaded From: https://www.spiedigitallibrary.org/conference-proceedings-of-spie on 10 Dec 2021
Terms of Use: https://www.spiedigitallibrary.org/terms-of-use

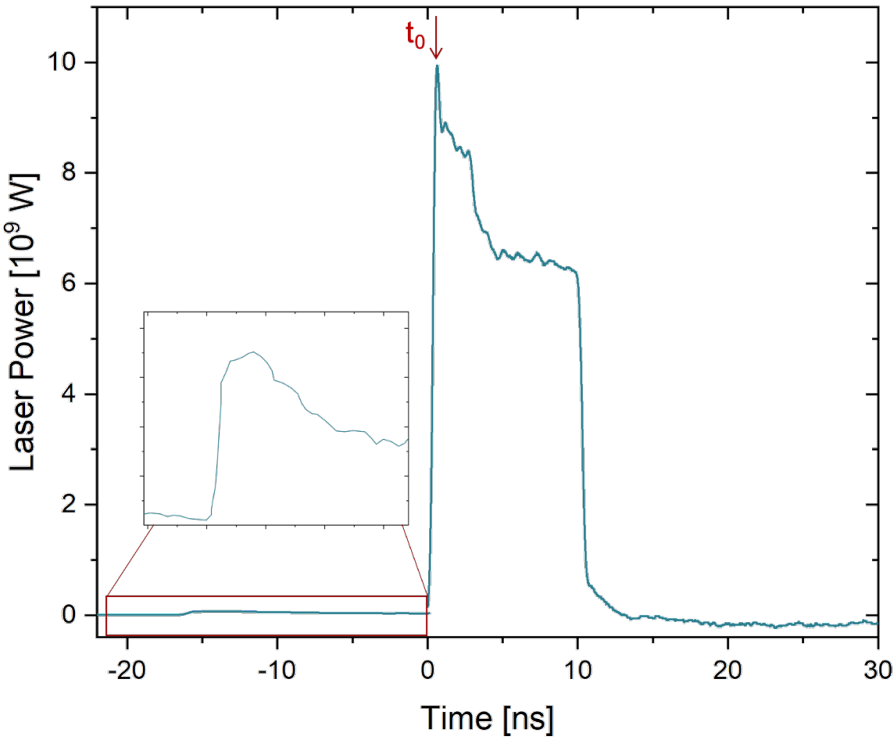


Fig 2 Oscilloscope trace of the shape of the optical laser shock drive profile for run 246. The inset plot shows the shape of the pre-pulse (1J), i.e., a low-intensity laser pulse that drives compression at moderate pressure prior to the main flat top drive pulse. t0 is the start of the main compressive wave on the sample.

The XFEL four-pulse train at LCLS provides four bursts of x-ray pulses,[23] which enabled us to image in-situ, the changes in the sample's structure on the UXI camera. The pulses have adjustable time separation (see Fig. 3) and captured the x-ray phase-contrast images of the sample in real time during shock compression. While four frames were recorded with the UXI, the third frame had consistently low signal either due to low x-ray pulse intensity or fluctuating timing, and therefore it is not shown here.

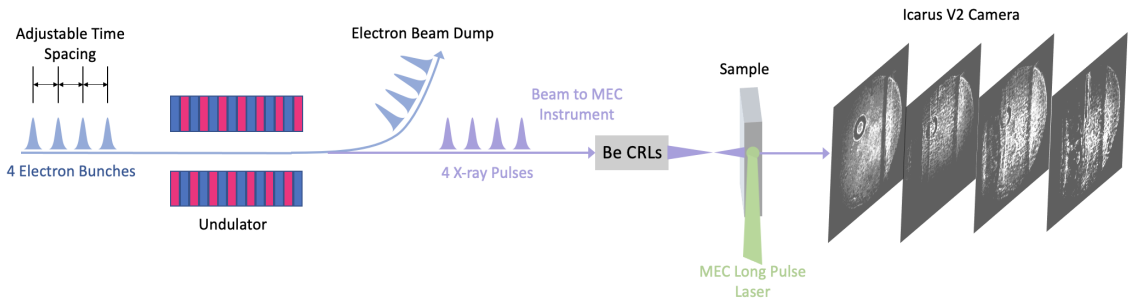


Fig 3 A schematic describing the XPCI setup and the pulse separation the the XFEL four-pulse train at LCLS. (Figure adapted from Hart et al.[12])

.

Downloaded From: https://www.spiedigitallibrary.org/conference-proceedings-of-spie on 10 Dec 2021
Terms of Use: https://www.spiedigitallibrary.org/terms-of-use

The highly coherent XFEL beam and the Icarus V2 detector enabled time-resolved phase-contrast imaging with high spatial resolution. To obtain high resolution images, we used 40 Beryllium compound refractive lenses (50 μm radius of curvature and 300 μm aperture) to focus the XFEL pulses to a 150 nm spot FWHM 197 mm behind the optics, which expands to 275 μm at the photoresist SU-8 samples 158 mm behind the focus. We calibrated the spot size using a 12.5 μm pitch nickel grid.

Since a single target is destroyed within microseconds for each laser shock drive, we loaded several samples on cartridges at a time. The setup included a motorized stage with six degrees of freedom, which gave an area of 150 mm x 25 mm to mount targets. We stationed the Icarus V2 detector 4.583 meters after the samples at the end of a long flight tube connected to the samples and capped with a polyamide window. The effective magnification of the setup is 29 giving us an effective pixel size of 850 nm, much larger than the potential resolution of 150 nm from the nanofocused spot. This resolution is pixel- size and geometry-limited in our experimental configuration due to the larger field of view desired (275 μm) on the sample.

4 Data Analysis

At the MEC instrument we recorded multiple runs with the Icarus V2 camera. However, during the alignment of the system some pixels on one half of the detector were exposed to unattenuated light, damaging part of the detecting area (possibly caused by a spurious reflection of the shock laser drive or XFEL beam being unattenuated). These damaged image areas can be seen in run 292 involving this fast-framing detector. An example of the inpainting algorithm is illustrated in Fig. 4 using a static frame from run 292. We applied this algorithm to three additional frames for run 292 and refer these inpainted images from here on out. To fill the damaged areas in the images, both the texture and the geometry of the images were considered. Through the use of the built-in exemplar-based inpainting algorithm in MATLAB, we were able to fill in dead pixels by simultaneously propagating textures and geometry. Fig. 4 demonstrates the efficiency of the inpainting algorithm that has been applied to the images presented in the following (Fig. 5). This algorithm is based on the work of Criminisi et al.[24] The benefit of using this algorithm is that it does not suffer from blurring via diffusion processes in large damaged regions.

Downloaded From: https://www.spiedigitallibrary.org/conference-proceedings-of-spie on 10 Dec 2021
Terms of Use: https://www.spiedigitallibrary.org/terms-of-use

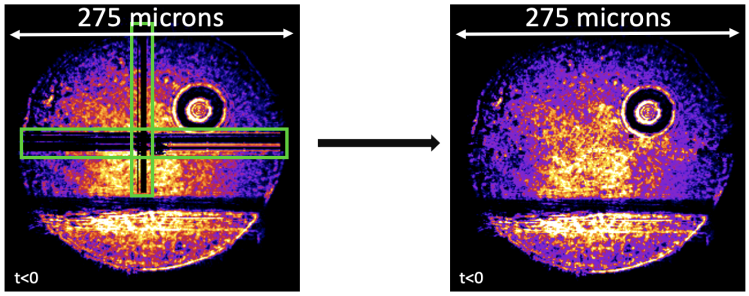


Fig 4 Example of inpainting of damaged pixels in run 292 where we captured a series of x-ray phase-contrast images with the Icarus V2 fast-framing detector. The left image represents a real image we recorded on the Icarus V2 with damaged rows and columns shown with green boxes. The right image displays the results of exemplar-based inpainting.[24]

The exemplar-based algorithm begins by a user locating a specific region to be fixed or filled. This is the 'target' region, while everything else in the image is the 'source' region. The priority of filling in this algorithm is based on a confidence and data term, which helps determine the priority of the patch to be filled in the 'target' region. The patch with the highest priority in the 'target' region is chosen to be filled from the most similar patch in the 'source' region. This best patch is found by the sum of square differences (SSD). Simultaneously, the data term propagates geometry and the confidence term propagates textures into that 'target' region. There is a trade-off between the confidence and data terms, such that the linear structures or geometry is synthesized first before textures fill in the dead pixels. The confidence value is updated and the process repeats until the 'target' region is entirely filled.

Downloaded From: https://www.spiedigitallibrary.org/conference-proceedings-of-spie on 10 Dec 2021
Terms of Use: https://www.spiedigitallibrary.org/terms-of-use

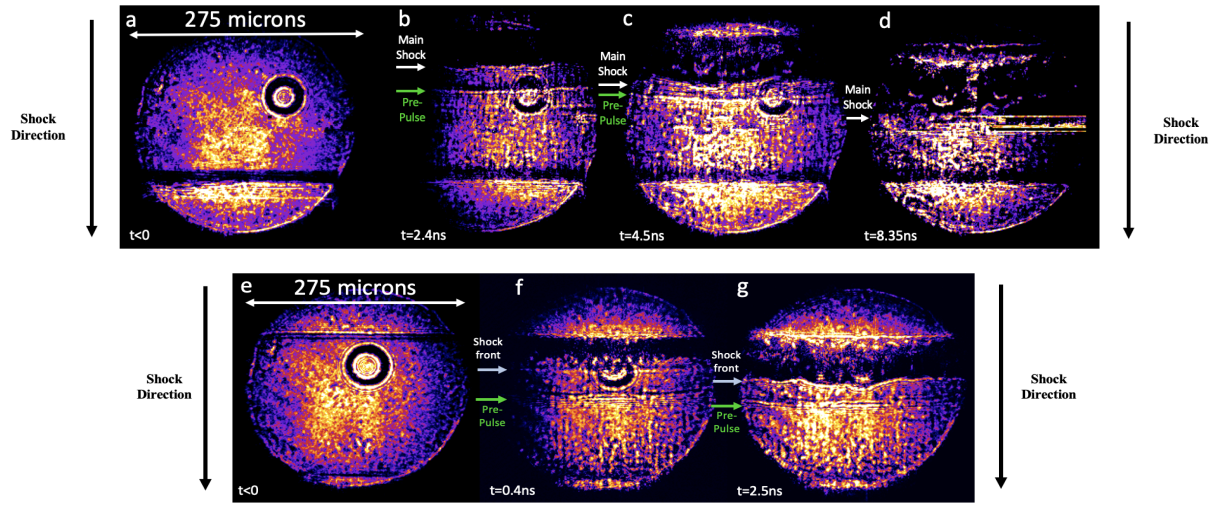


Fig 5 (a-d) X-ray phase-contrast images for run 292. A 10 ns flat-top pulse was used to drive a shock wave into the SU-8 sample. The t<0 frame is the static pre-drive image. The XFEL beam spot diameter at the sample position is 275 μm. Three frames of the four-pulse train x-ray phase-contrast images are shown from LCLS at 8.23 keV of a SU-8 photoresist sample during passage of a laser-driven shockwave. Relative timing is shown in the lower corner of each frame. A weak shock from the pre-pulse, indicated by a green arrow, travels downward at a speed of 2.95+/-0.3 km/s, resulting in a pressure of ∼1.4+/-0.6 GPa. The pre-pulse is followed by the main pulse that travels at a speed of 9.44+/-0.6 km/s, resulting in a pressure of ∼50+/-9 GPa. (e-f) X-ray phase-contrast images for run 295. A static pre-shot (t<0) and two dynamic images from the four pulse train were collected. The pre-pulse travels as a speed of 3.54+/-0.3 km/s, resulting in a pressure of ∼2.7+/-0.8 GPa. The main pulse travels at a speed of 10.62+/-1.0 km/s, resulting in a pressure of ∼71+/-19 GPa.

As shown in Fig. 5, we can see that the Icarus V2 is capable of capturing multiple frames from a single sample as it is laser shocked on the few nanosecond time scale. We note that the Icarus V2 camera was able to record and readout four frames, but low x-ray pulse intensity or fluctuating timing caused one frame in run 292 and two frames in run 295 to have very low signal. As a result, those frames are not included.

As can be seen with images (a-d) in Fig. 5, we retrieved four x-ray phase-contrast images of a SU-8 sample, a low-density polymer, with a 40 μm hollow glass void and we can observe the changes taking place in the sample upon passage of a shock wave on the nanosecond scale. In frame (a) in Fig. 5, we have a static image, where we can clearly see a micro-void. Then, 2.4 ns later in frame (b) in Fig. 5, we can see two shock waves: first a weak elastic shock propagating through the material (indicated by a green arrow), maintaining its planar shape as it passes through the void; it is also worth noting that the void geometry is not altered after interaction with this first compressive wave. After 4.5 ns (frame c in Fig. 5) since the initial XFEL pulse, the second shock front (indicated by a white arrow), i.e., the one caused by the main flat top pulse (see Fig. 2), interacts with the void altering the material structure. This high pressure wave induces strong changes in

Downloaded From: https://www.spiedigitallibrary.org/conference-proceedings-of-spie on 10 Dec 2021
Terms of Use: https://www.spiedigitallibrary.org/terms-of-use

material density and a dark band surrounding the shock front is visible in the data.

As seen from (e-g) in Fig. 5, the Icarus V2 camera captured three frames of another SU-8 photoresist sample. In this run, we were able to only collect two dynamic frames since we had low signal due to low x-ray pulse intensity or fluctuating timing. In the first frame, we have a static image with a glass micro-void. Then 0.4 ns after the initial pulse (frame f in Fig. 5), we can see both the low- and the main high-pressure waves (indicated by green and white arrows). At 2.5 ns (frame g in Fig. 5), the distance between the low- and the high-pressure wave front has diminished, confirming that the second wave travels at a higher speed. From frame (g) in Fig. 5, we can also appreciate the changes in the shock front profile, that does not appear planar most likely because of the interaction with the void. This uneven compression could give rise to hydrodynamic instabilities, laser boring, ablation layer nonuniformities, etc.

In these runs, the shock velocity (Us) for both the low- and high-pressure shock waves has been estimated by analyzing the motion of the shock front in successive frames acquired from a single sample. The equation of state of polyamide, a polymer analogue to the SU-8 photoresist and of comparable density ($1.146 g/cm^3$) was used to infer the pressure state reached along the Hugoniot curve upon shock compression.[25] For run 292, the pre-pulse generates a weak elastic shock wave that propagates through the sample with a shock speed of 2.95+/-0.3 km/s, corresponding to a pressure around 1.4+/-0.6 GPa; the main pulse generates a higher pressure state, i.e., 50+/-9 GPa, with an estimated shock speed of 9.44+/-0.6 km/s. Similarly, for run 295, the pre-pulse generates a weak elastic shock wave that propagates through the sample with a shock speed of 3.54+/-0.3 km/s, corresponding to a pressure around 2.7+/-0.8 GPa; the main pulse generates a higher pressure state, i.e., 71+/-19 GPa, with an estimated shock speed of 10.62+/-1.0 km/s. From these runs we see that the pre-pulse generated a low-energy elastic shock wave, compressing the sample to an initial pressure of a few ($\sim$1-3) GPa, while the main pulse produced higher pressure shock states up to $\sim$50-70 GPa. Despite having the same nominal pulse profile, the shot-to-shot variation and the presence of the pre-pulse made it difficult to reproduce consistently the same pressure conditions in the samples over different runs.

The turbulent appearance of the dark band is due to the occurrence of the laser-plasma instabilities and other hydrodynamic instabilities in the shock front. The origin of the dark band visible in the data could be, as suggested by PCI simulation (see Fig. 6), the refraction and diffraction phenomena taking place at the shock front. Mitigation of this dark band can be achieved with higher x-ray photon energies, which is shown in Fig. 7. Additionally, there are small fragments that appear in the dark band after the optical pulse propagates through part of the material. These fragment structures in the dark band could be explained by laser boring into the sample or imperfections in the ablation layer.

Downloaded From: https://www.spiedigitallibrary.org/conference-proceedings-of-spie on 10 Dec 2021
Terms of Use: https://www.spiedigitallibrary.org/terms-of-use

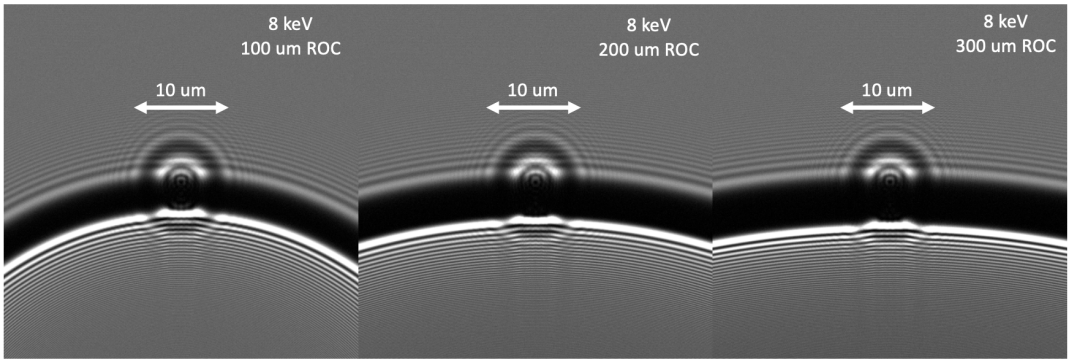


Fig 6 This simulation describes different radius of curvatures (ROCs) of the shock front for 8 keV x-rays and its impact on void collapse.

The curvature of the shock front, the density jump between shocked and unshocked material, the size of the void, and the x-ray probe wavelength are all contributing factors that affect our ability to image the void as a shock or compressive wave propagates through it. To better interpret the experimental data, we performed phase-contrast imaging simulations of synthetic phantom objects to reproduce our experimental geometry. A density jump with varying radius of curvature interacting with a spherical void was used to mock up the shock front for compression at varying pressures, as shown in Fig. 6. Increasing the simulated 'shock' radius of curvature increases the phase jump, increasing the dark band width due to refraction. These same phantom phase-contrast simulations, depicted in Fig. 7 also indicate that using higher x-ray photon energies will reduce the width and darkness of the band, allowing better visibility of the void during shock passage.

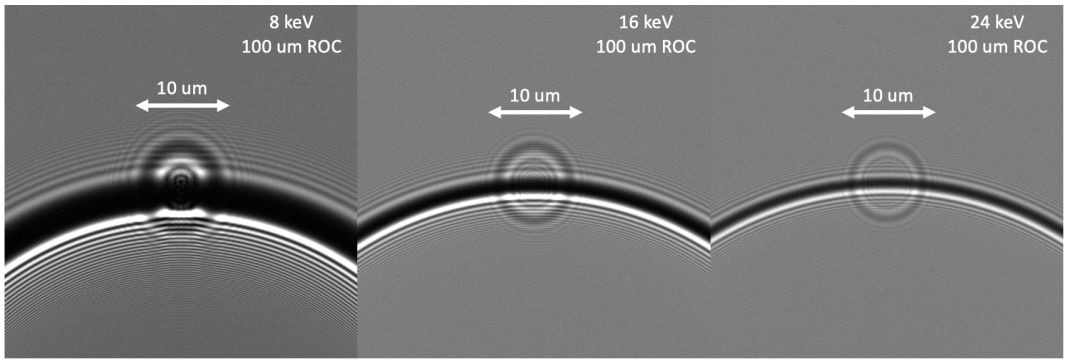


Fig 7 A simulation that demonstrates that with increasing x-ray photon energy, the dark band width is reduced in size. This enables better visibility of the void undergoing shock compression. In this example, the same radius of curvature (ROC) for the shock wave is used.

5 Conclusions

Here, we used the XFEL four-pulse train at LCLS to image dynamically changing materials under laser shock compression at the MEC instrument for the first time, allowing us

Downloaded From: https://www.spiedigitallibrary.org/conference-proceedings-of-spie on 10 Dec 2021
Terms of Use: https://www.spiedigitallibrary.org/terms-of-use

to make preliminary but substantive comparisons with simulations of void collapse. With the unique high flux and brilliance from the XFEL, we obtained multi-frame x-ray phase-contrast images with high spatial and temporal resolution captured by the Icarus V2 fast-framing camera. The Icarus V2 camera is beneficial to XFEL science as it is primed for burst mode data collection and compatible with the time frames for dynamic compression, on the order of a few nanoseconds.[11] Examining the effect of material heterogeneities, like micro-voids, on material properties during the passage of a laser-driven shock wave is important for benchmarking the performances of ICF energy materials at extreme conditions. Our novel method for in-situ ultrafast imaging will allow characterization of void response to laser shock compression will and provide fundamental insight on how to minimize the growth of instabilities that occur at the micro scale. Now it will be possible to develop better predictive models and improve materials design with information gathered from materials dynamically changing in extreme conditions.

LCLS has the capability of producing x-ray pulses with a temporal spacing as short as 350 ps.[13,14] We anticipate using new hard x-ray sensor UXI detectors currently in production in future runs to study void-shock interactions at the sub-nanosecond time scale. This will allow imaging of processes that evolve at an even faster timescales with high resolution, providing novel insights on how the voids size affects void collapse, collapse rates, jetting formation, interaction with the shock front, formation of hot spots, and plasma properties. This will enable us to see through the dark band that was previously mentioned and will give information on microstructural features that appear in the void collapse process.

DISCLOSURES

There are no conflicts of interest among any of the authors.

ACKNOWLEDGEMENTS

The authors would like to thank the accelerator team for providing the four-pulse trains. This research was performed at the Linac Coherent Light Source (LCLS) at the SLAC National Accelerator Laboratory. LCLS is operated for the US Department of Energy Office of Science by Stanford University. Additional support from the DOE Office of Science was given towards the operation of the MEC instrument. Part of this work was performed at the Stanford Nano Shared Facilities (SNSF), supported by the National Science Foundation under award ECCS-2026822. A.G. and S.P. were supported by DOE Office of Science, Fusion Energy Science ECA.

Downloaded From: https://www.spiedigitallibrary.org/conference-proceedings-of-spie on 10 Dec 2021
Terms of Use: https://www.spiedigitallibrary.org/terms-of-use

References

1 A. E. Gleason, C. A. Bolme, H. J. Lee, *et al.*, "Ultrafast visualization of crystallization and grain growth in shock-compressed SiO2," *Nature Communications* **6** (2015).

2 E. E. McBride, A. Krygier, A. Ehnes, *et al.*, "Phase transition lowering in dynamically compressed silicon," *Nature Physics* **15**(1) (2019).

3 D. Kraus, J. Vorberger, A. Pak, *et al.*, "Formation of diamonds in laser-compressed hydrocarbons at planetary interior conditions," *Nature Astronomy* **1**(9) (2017).

4 C. E. Wehrenberg, D. McGonegle, C. Bolme, *et al.*, "In situ X-ray diffraction measurement of shock-wave-driven twinning and lattice dynamics," *Nature* **550**(7677) (2017).

5 B. Nagler, B. Arnold, G. Bouchard, *et al.*, "The Matter in Extreme Conditions instrument at the Linac Coherent Light Source," *Journal of Synchrotron Radiation* **22** (2015).

6 S. H. Glenzer, L. B. Fletcher, E. Galtier, *et al.*, "Matter under extreme conditions experiments at the Linac Coherent Light Source," (2016).

7 V. A. Smalyuk, C. R. Weber, O. L. Landen, *et al.*, "Recent and planned hydrodynamic instability experiments on indirect-drive implosions on the National Ignition Facility," *High Energy Density Physics* **36** (2020).

8 D. S. Clark, M. M. Marinak, C. R. Weber, *et al.*, "Radiation hydrodynamics modeling of the highest compression inertial confinement fusion ignition experiment from the National Ignition Campaign," *Physics of Plasmas* **22**(2) (2015).

9 A. B. Zylstra, D. T. Casey, A. Kritcher, *et al.*, "Hot-spot mix in large-scale HDC implosions at NIF," *Physics of Plasmas* **27**(9) (2020).

10 L. A. Pickworth, B. A. Hammel, V. A. Smalyuk, *et al.*, "Visualizing deceleration-phase instabilities in inertial confinement fusion implosions using an "enhanced self-emission" technique at the National Ignition Facility," *Physics of Plasmas* **25**(5) (2018).

11 E. R. Hurd, A. C. Carpenter, M. S. Dayton, *et al.*, "Performance characterization of a four-frame nanosecond gated hybrid CMOS image sensor," (2018).

12 P. A. Hart, A. C. Carpenter, L. D. Claus, *et al.*, "First x-ray test of the Icarus nanosecond-gated camera," (2019).

13 F. J. Decker, R. Akre, A. Brachmann, *et al.*, "A demonstration of multi-bunch operation in the LCLS," in *FEL 2010 - 32nd International Free Electron Laser Conference*, (2010).

14 Y. Sun, F. J. Decker, J. Turner, *et al.*, "Pulse intensity characterization of the LCLS nanosecond double-bunch mode of operation," *Journal of Synchrotron Radiation* **25**(3) (2018).

15 Y. Shi and D. W. Brenner, "Jetting and Detonation Initiation in Shock Induced Collapse of Nanometer-Scale Voids," *Journal of Physical Chemistry C* **112**(16) (2008).

16 "ALE3D Void Collapse Simulation." https://wci.llnl.gov/simulation/computer-codes/ale3d.

Downloaded From: https://www.spiedigitallibrary.org/conference-proceedings-of-spie on 10 Dec 2021
Terms of Use: https://www.spiedigitallibrary.org/terms-of-use

17 L. Claus, L. Fang, R. Kay, *et al.*, "An overview of the Ultrafast X-ray Imager (UXI) program at Sandia Labs," in *Target Diagnostics Physics and Engineering for Inertial Confinement Fusion IV*, **9591** (2015).

18 L. D. Claus, M. Sanchez, G. A. Robertson, *et al.*, "Design and characterization of an improved 2 ns multi-frame imager for the ultra-fast x-ray imager (UXI) program at Sandia National Laboratories," (2017).

19 H. Chen, N. Palmer, M. Dayton, *et al.*, "A high-speed two-frame, 1-2 ns gated X-ray CMOS imager used as a hohlraum diagnostic on the National Ignition Facility (invited)," in *Review of Scientific Instruments*, **87**(11) (2016).

20 M. Dayton, A. Carpenter, H. Chen, *et al.*, "A characterization technique for nanosecond gated CMOS x-ray cameras," in *Target Diagnostics Physics and Engineering for Inertial Confinement Fusion V*, **9966** (2016).

21 D. Damiani, M. Dubrovin, I. Gaponenko, *et al.*, "Linac Coherent Light Source data analysis using psana," *Journal of Applied Crystallography* **49** (2016).

22 J. P. Duris, J. P. Macarthur, J. M. Glownia, *et al.*, "Controllable X-Ray Pulse Trains from Enhanced Self-Amplified Spontaneous Emission," *Physical Review Letters* **126**(10) (2021).

23 F. Krausz and M. Ivanov, "Attosecond physics," *Reviews of Modern Physics* **81**(1) (2009).

24 A. Criminisi, P. Pérez, and K. Toyama, "Region filling and object removal by exemplar-based image inpainting," *IEEE Transactions on Image Processing* **13**(9) (2004).

25 M. Carter, W.J., *Hugoniot equation of state of polymers*, United States. Dept. of Energy. ;, Washington, D.C. : (1995).

Downloaded From: https://www.spiedigitallibrary.org/conference-proceedings-of-spie on 10 Dec 2021
Terms of Use: https://www.spiedigitallibrary.org/terms-of-use